Article

Depolarization Measurement through a Single-Mode Fiber-Based Endoscope for Full Mueller Endoscopic Polarimetric Imaging

Colman Buckley, Marc Fabert and Dominique Pagnoux *

University of Limoges, CNRS, Xlim, UMR7252, F-87000 Limoges, France
* Correspondence: dominique.pagnoux@xlim.fr

Abstract: Coupled to endoscopic techniques, Mueller polarimetry has been proven to be promising for early detection of certain diseases which affect biological tissues of inner organs. However, the depolarization power which is one of the most informative polarimetric characteristics cannot be directly measured through a fiber endoscope. For evaluating this quantity, we propose a method based on the Lu–Chipman decomposition of the averaged sum of the Mueller matrices of neighboring pixels. The principle is well supported by numerical simulations. Depolarization powers of Spectralon and of different areas of a biological sample are also successfully evaluated.

Keywords: Mueller polarimetry; depolarization; optical fibers; single-mode fiber; endoscopy

1. Introduction

Over the past twenty years, polarization imaging techniques have been demonstrated to be very attractive for non-destructive characterization of materials, in particular biological tissues [1–4]. Compared to intensity-based measurements, optical polarimetry provides additional information on the structure of tissues at the submicronic scale, especially fibrillar type I collagen [5,6].

Among the existing techniques, Mueller polarimetry has attracted a special interest in recent years, as it is the only one capable of measuring all the polarimetric effects experienced by a probing beam when it interacts with the tissue (sample): linear and/or circular retardance, linear and/or circular diattenuation, and depolarization [7]. From these quantities, information on the structural anisotropy (birefringence) and on the disorganization of the fibers arrangement in type I collagen can be drawn. Thereby, since the fibrillar structure of type I collagen can be affected due to the development of pathologies such as fibrosis or certain cancers, Mueller polarimetric imaging has often been proposed for early diagnosis of such diseases and for discriminating between healthy and pathological regions [8–13].

The principle of Mueller polarimetry has already been extensively presented in the literature [7,14]. In short, it consists of addressing four successive predefined polarization states from a Polarization State Generator (PSG) on the sample, and in analyzing each transmitted state via four successive configurations of a Polarization States Analyser (PSA). By means of relevant linear combinations of the 16 intensities measured after the PSA, it makes it possible to build a 4 × 4 matrix (so-called Mueller matrix M) which relates any incident polarization state (represented by its 4 elements Stokes vector S) to the corresponding transmitted polarization state (represented by its 4 elements Stokes vector S'), by means of the relation:

$$S' = M.S \tag{1}$$

The Mueller matrix *M* represents the polarimetric response of the sample. To identify and quantify the specific polarimetric effects generated in this sample, *M* is generally decomposed into a product of matrices of pure polarimetric effects (so-called "basic" matrices in the following), under the assumption that they come one after the other in the sample. However, in practice, these effects are entangled in a complicated manner, generating intense debate in the scientific community concerning the most relevant order of the basic matrices in the product [15–18]. Nevertheless, the Lu–Chipman decomposition, which states that the probe beam successively undergoes diattenuation, then retardance, and finally depolarization, is the most widely agreed [19]. Therefore, the Mueller matrix *M* is decomposed as follows:

$$M = M_{\Delta}.M_{R}.M_{D} \tag{2}$$

where M_D, M_R and M_Δ are, respectively, the Mueller matrices of a diattenuator, a retarder and a depolarizer.

In view of clinical trials for early diagnosis of diseases on deep organs, inner Mueller polarimetric imaging is of major interest. For such application, the process must be coupled to a flexible fiber endoscope. In this case, one difficult challenge arises, which is to get rid of the uncontrollable and time-dependent changes of the polarization states of light when propagating in the fiber, both in the forward and the backward path. Only a few techniques have been reported in the literature to overcome this problem. Some of them provide only part of the requested polarimetric parameters [20–22]. Others can only achieve a single pixel measurement [23] or require a bulky and very sophisticated optical head including remote PSG and PSA, not suitable for application in usual endoscopy [24].

As a solution, we reported in a previous paper a method for measuring the full Mueller matrix of the sample through a single-mode fiber, so-called "two-wavelength differential method (TWDM)" [25]. In brief, the method was based on the simultaneous measurements of the Mueller matrix M_1 of the fiber in double path at a wavelength λ_1, and that of the assembly "fiber + sample" (matrix M_2) at a very close wavelength λ_2. For enabling these two measurements, a dichroic mirror highly reflective at λ_1 and transparent at λ_2 was set at the distal end of the fiber. Thus, two probe beams at λ_1 and λ_2, respectively, simultaneously launched in the fiber, were separated by the dichroic filter, the former being directly reflected in the fiber and the latter exiting towards the sample. Part of this beam reflected by the sample was then recoupled into the fiber. The beams at λ_1 and λ_2 back guided by the fiber and transmitted through the PSA, were separated by a spectral filter, each wavelength being directed towards one intensity detector. Matrices M_1 and M_2 were deduced from the intensities measured for 16 combinations of the assembly PSG/PSA, at λ_1 and λ_2, respectively. Finally, as explained in detail in [25], the Mueller matrix of the sample was calculated from the matrices M_1 and M_2. In the implementation of the method reported in [25], we used two CW lasers emitting at λ_1 = 634 nm and λ_2 = 640 nm, respectively.

Let us note that light coupling in the fiber endoscope, in both directions, would be much easier with a large-core high numerical aperture multimode fiber. However, polarization changes along the propagation in a multimode fiber drastically depend on each guided mode. As these changes are not controllable nor measurable individually, multimode propagation cannot be tolerated in the fiber endoscope. For that reason, the TWDM can be implemented only with a single-mode fiber endoscope.

In order to perform polarimetric images by means of the TWDM through such a single-mode fiber endoscope, a scanning device compatible with the technique must be implemented. In the first demonstration reported in [25], we used a bulk scanner founded on x/y galvanometric mirrors. Later, to complete another stage towards an operational

endoscopic polarimetric imaging device, we developed a TWDM compatible endomicroscope, including a minimally invasive cylindrical microprobe (2.9 mm in diameter and 30 mm in length) at the end of a 2 m endoscopic fiber [26]. In this miniaturized device, for compactness and efficient filtering purposes, the dichroic filter was replaced by a Fiber Bragg Grating (FBG) photowritten at the output end of the fiber. On the other hand, the scanning operation of the sample was operated by means of a dual-axis resonant mechanical excitation of the extremity of the fiber which was attached in a piezoelectric tube (PZT) set inside the microprobe, as depicted in Figure 1. The beam exiting the fiber was focused on the sample by a micro-optic imaging system placed at the extremity of the probe. This device was able to acquire 4 × 4 Mueller polarimetric images with a frame rate of 1 image/2 s.
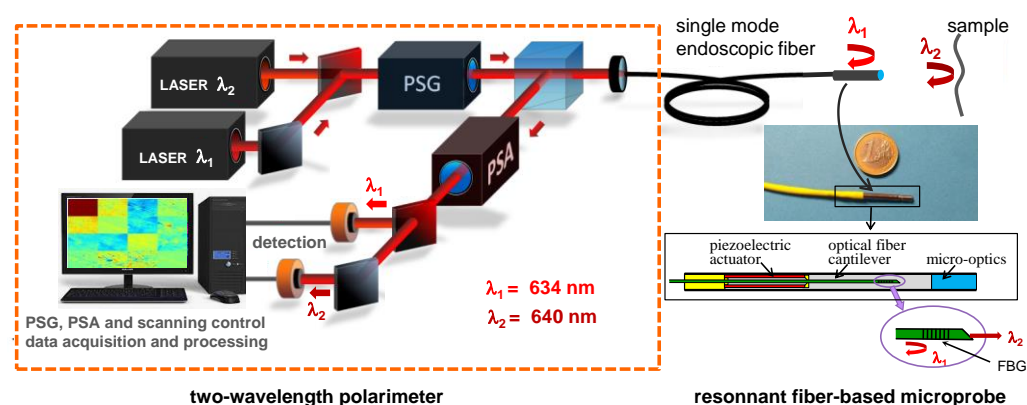

Figure 1. Schematic representation of an endomicroscope designed for achieving remote in situ Mueller polarimetric imaging by means of the two-wavelength differential method [26].

The TWDM has already been shown to allow effective and reliable measurements of linear and circular retardance and linear and circular diattenuation through a fiber endoscope [25,26]. However, the determination of another polarimetric quantity which is the spatial depolarization power of the sample is also of great interest for characterizing fibrillar tissues, as it is related to the degree of disorganization of the collagen fibers and fibrils [27]. In turn, it can reflect the existence of a possible pathology and even the stage of this pathology. For example, the measurement of this parameter on the cervix can help for the evaluation of the risk of prematurity [28]. It can also help for the early diagnosis of specific cancerous tumors or fibrosis on different external or internal organs [29]. In particular, depolarization measurements can help distinguishing between benign neurofibroma and cancerous cell carcinoma or melanoma [1,30]. Other recent works have shown promising applications of such measurements for characterizing prostate adenomia [31] and colon tumors [32,33]. Classically, this depolarization power is calculated from the matrix M_Δ extracted from the Lu–Chipman decomposition of M (see Equation (2)), as reminded in more details in Section 2. However, at this point, we must note a profound difference between measures performed by means of a classical free-space Mueller imaging system and those achieved by scanning the sample with a focused beam from a single-mode fiber endoscope. Indeed, when using a free-space Mueller imaging system, the entire imaged area of the sample is illuminated at the same time by a large probe beam. Thus, in the case of spatial depolarizing sample, the light detected by each pixel of the camera may include possible scattered incoherent contributions which had entered the sample at different points of this illuminated area. For that reason, non-zero depolarization can be measured by any pixel of the camera. On the contrary, when a single-mode fiber endoscope is used, the Gaussian beam exiting the fiber at the distal end is focused on a very small area of the sample at a given time. Typically, the mode field diameter of the probe beam in our fiber endoscope (diameter of the core ~3.5 μm) is ~4 μm and, as the magnification of the optical system is ~1, it produces an enlightened disk of only ~4

µm in diameter on the sample. As a result, only light entered in this area and backscattered from the same area can be collected by the fiber, with no incoherent contribution. Furthermore, the collected light is coupled in the fundamental LP$_{01}$ mode of the fiber which is linearly polarized all over its cross section. Thus, the backward beam which is analyzed by the PSA is totally polarized. In other words, at any time, no depolarization can be directly measured through a single-mode fiber endoscope.

In this paper, we propose a method for overcoming the major issue of measuring the depolarization ability of the sample when a single-mode fiber is used for endoscopic Mueller polarimetry. This method is based on the approach reported by Gil et al. in [34], where the depolarization induced by an area of the sample can be considered as equivalent to that resulting from the parallel combination of contributions of several non-depolarizing sub-areas. In the next section, we depict this method in more detail, and we show results of some related numerical simulations. In Section 3, we first describe the process used for implementing the method in our TWDM-based endoscopic Mueller polarimeter. Then, we report experimental measurements of depolarization power performed on different manufactured and biological samples and we discuss these results.

2. Method and Numerical Simulations

The polarization state of any optical beam can be described by means of its Stokes vector S:

$$S = \begin{pmatrix} S_0 \\ S_1 \\ S_2 \\ S_3 \end{pmatrix} \tag{3}$$

where S_0, S_1, S_2, and S_3 denote the four Stokes vector parameters [35]. The degree of polarization (DOP) of this beam represents the fraction of the electromagnetic wave which is fully polarized. It is given by [35]:

$$DOP = \frac{\sqrt{S_1^2 + S_2^2 + S_3^2}}{S_0} \tag{4}$$

Then, $DOP = 1$ for a fully polarized beam, $DOP = 0$ for a totally depolarized beam and $0 < DOP < 1$ for a partially depolarized beam.

On the other hand, the Mueller matrix M_Δ of a pure partially depolarizing sample (partial depolarizer) is written in the form:

$$M_\Delta = \begin{pmatrix} 1 & 0 & 0 & 0 \\ 0 & a & 0 & 0 \\ 0 & 0 & b & 0 \\ 0 & 0 & 0 & c \end{pmatrix} \quad |a|,|b|,|c| \le 1 \tag{5}$$

where $(1 - |a|)$, $(1 - |b|)$, and $(1 - |c|)$ are the depolarization factors, describing the depolarizing ability of the depolarizer, which, respectively, affect the Stokes parameters S_1, S_2, and S_3 of the incident beam. More precisely, M_Δ is the Mueller matrix of a partial depolarizer which reduces the DOP of an incident horizontal or vertical linearly polarized light by a factor $|a|$, the DOP of an incident 45° or 135° linearly polarized light by a factor $|b|$, and the DOP of an incident circularly polarized light by a factor $|c|$ [36].

After interaction with a pure partial depolarizer (Mueller matrix M_Δ), the Stokes vector S of an incident beam (Equation (3)) is changed in a new Stokes vector S':

$$S' = M_{\Delta}.S = \begin{pmatrix} S_0 \\ a.S_1 \\ b.S_2 \\ c.S_3 \end{pmatrix} \qquad (6)$$

The *DOP* of the transmitted beam (noted *DOP′*) is then, according to Equation (4):

$$DOP' = \frac{\sqrt{a^2 S_1^2 + b^2 S_2^2 + c^2 S_3^2}}{S_0} \qquad (7)$$

When $a = b = c$, the depolarizer is uniform and it reduces the *DOP* of any incident beam by a factor a [36]. If $a = b = c = 1$, the sample is a non-depolarizing element and *DOP′* = *DOP*. At the opposite, if $a = b = c = 0$, the sample is an ideal depolarizer and *DOP′* = 0 whatever the degree of polarization of the incident beam.

Different metrics can be used to quantify the depolarizing ability of a medium, such as the Cloud entropy [37], the depolarization index [34], or the differential depolarization index [38]. Among these metrics, we select the depolarization power Δ, which is of particular interest as it indicates the averaged depolarization capability of a depolarizer [19]. It is defined as the mean value of the depolarization factors, and thus it is expressed as:

$$\Delta = 1 - \frac{|a| + |b| + |c|}{3} \qquad (8)$$

We can notice that both Δ, and *DOP′* compared to *DOP*, reflect the ability of the sample to depolarize light. However, there is no direct relationship between Δ and *DOP′*, except in the case where the incident beam is fully polarized and the sample is a uniform depolarizer. In this case, $\Delta = 1 - |a|$ and $DOP' = |a|$, i.e., $DOP' = 1 - \Delta$.

In the pioneer work published by H.C. Van de Hulst in 1957, it was shown that a depolarizing optical system is optically equivalent to a system composed of a parallel combination of several non-depolarizing optical systems [39]. Therefore, since the Mueller matrix of a parallel combination of optical systems is the sum of the Mueller matrices of the systems which form the parallel combination, a depolarizing Mueller matrix can be written as the sum of various non-depolarizing Mueller matrices [34]. In other words, the depolarization power of a given area A of a sample can be evaluated using the coefficients a, b, and c of the matrix M_Δ extracted from the decomposition of the Mueller matrix $\bar{M}$ given by:

$$\bar{M} = \frac{1}{n} \sum_{i=1}^{n} M_i \qquad (9)$$

where M_i is the Mueller matrix of an elementary non-depolarizing area A_i of A, A being the juxtaposition of the n areas $A_{i(i=1, n)}$.

Let us note that a similar approach was used to investigate the depth-resolved depolarization properties of human retina [40,41] or skin tissue [30] by means of polarization sensitive optical coherent tomography (PS-OCT). In these studies, the objective was to determine the degree of polarization of the transmitted beam *DOP′*. However, OCT being a coherent method, one issue in PS-OCT is similar to the one encountered with our endoscopic technique, i.e., light detected from one single speckle grain is always fully polarized. Thus, in PS-OCT, *DOP′* cannot be directly measured. To overcome this infeasibility, the Stokes vectors of adjacent speckle grains (pixels) were first measured and, considering that these adjacent speckle grains are uncorrelated, an average Stokes vector was determined over a given area. Each parameter $\overline{S_0}$, $\overline{S_1}$, $\overline{S_2}$ and $\overline{S_3}$ of this vector was

the mean value of the corresponding parameters of the individual Stokes vectors measured in this area. Then, a quantity called degree of polarization uniformity (*DOPU*) was defined as:

$$DOPU = \frac{\sqrt{\overline{S_1}^2 + \overline{S_2}^2 + \overline{S_3}^2}}{\overline{S_0}} \tag{10}$$

Assuming that the probe beam is fully polarized, *DOPU* reflects the random variation of the polarization states of adjacent speckle grains and it is closely related to the desired *DOP'*. In other words, it might be regarded as a spatially-averaged degree of polarization allowing a quantitative evaluation of the magnitude of the depolarization induced by the sample.

Inspired by the above works, we propose in this paper to extract the depolarization power of a sample from numerical processing of the Mueller matrices of neighboring pixels measured by means of our TWDM-based endoscopic Mueller polarimeter. The process is the following:

- The Mueller matrix of each pixel of an image of the sample ("elementary matrix") is first measured and registered following the procedure previously reported in [25]. As already stated, since the optical fiber is single-mode, each elementary matrix is a non-depolarizing matrix;
- Then, for each pixel P, the average Mueller matrix over adjacent pixels is calculated, these pixels being those within a floating square window around P, as depicted in Figure 2. The size of this floating window, chosen beforehand, is $N = (2n + 1)^2$ pixels, n being the number of considered rings of pixels around P;
- Each average Mueller matrix is decomposed by means of the Lu–Chipman method, in order to extract the associated depolarization matrix M_Δ whose form is given in Equation (5);
- The depolarization power Δ of each pixel is finally calculated by means of Equation (8), and a pixelated image of $\Delta(x,y)$ is plotted.
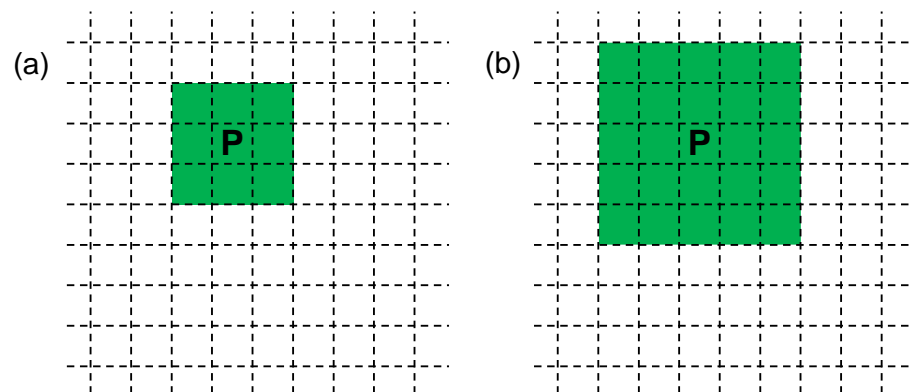

Figure 2. Pixels (green) in which Mueller matrices are averaged in order to calculate the depolarization power associated to the central pixel P. (**a**) considering 1 ring of pixels surrounding P (9 averaged Mueller matrices); (**b**) considering 2 rings of pixels surrounding P (25 averaged Mueller matrices).

Prior to experimental measurements and processing, we numerically studied the evolution of the depolarization power according to the diversity of the averaged Mueller matrices. Since biological tissues mainly present phase retardation in addition to depolarization, we first considered only elementary Mueller matrices of linear retarders. For better precision, we involved a large number of retarders (N = 1000), the retardance and the eigenaxes orientation of each being randomly drawn in a continuous uniform distribution, within a predefined range

Ψ_δ set around a central value δ_0 for the retardance, and within a predefined range Ψ_θ set around $\theta_0 = 0°$ regarding the eigenaxes orientation. For each retarder, we computed the corresponding elementary Mueller matrix and then we calculated the average Mueller matrix $\bar{M}$. Afterwards, $\bar{M}$ was decomposed by the Lu–Chipman method in order to extract the pure depolarization matrix from which the depolarization power Δ was finally calculated. In Figure 3, we plot Δ as a function of Ψ_δ and Ψ_θ, for 3 different values of the central retardance δ_0. In Table 1, we report Δ for some particular values of δ_0, Ψ_δ, and Ψ_θ.
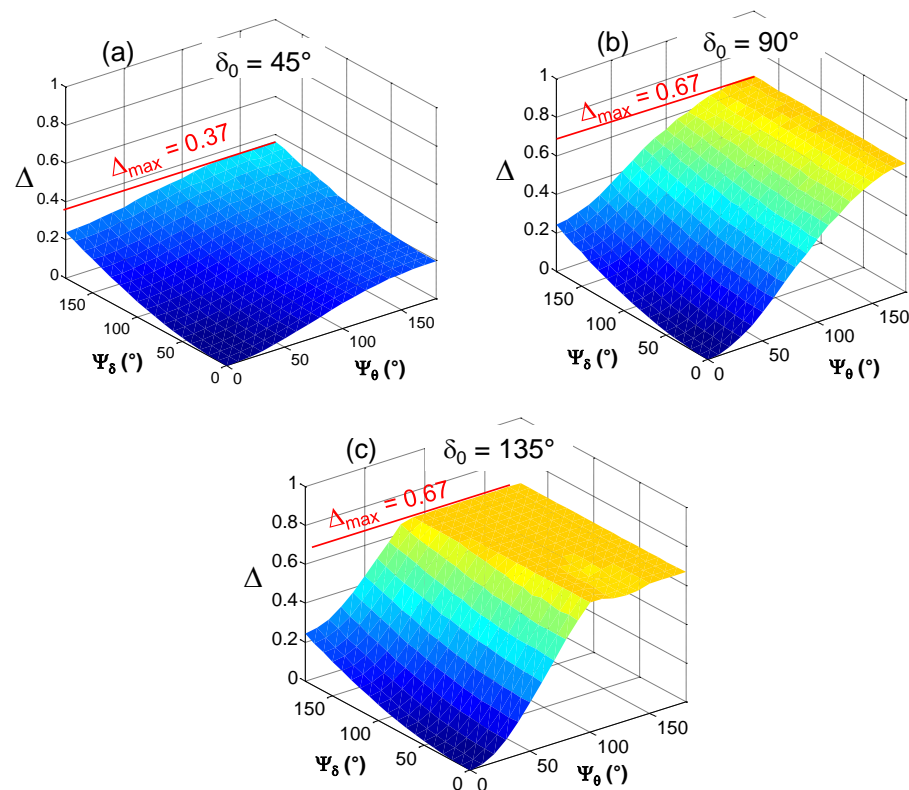

Figure 3. Depolarization power Δ of the average Mueller matrix of 1000 elementary Mueller matrices of neighboring pure retarders, calculated as a function of the variation range of the retardance Ψ_δ and of the variation range of the orientation of the eigenaxes Ψ_θ of these retarders. Three central values δ_0 of the retardance are considered: (**a**) $\delta_0 = 45°$; (**b**) $\delta_0 = 90°$; (**c**) $\delta_0 = 135°$.

Table 1. Depolarization power for particular values of Ψ_δ, δ_0, and Ψ_θ.

Ψ_θ (°)	Ψ_δ (°)		$\delta_0 = 45°$	$\delta_0 = 90°$	$\delta_0 = 135°$
0	0		0	0	0
0	90		0.07	0.07	0.07
0	180	$\Delta \rightarrow$	0.24	0.24	0.24
90	90		0.17	0.42	0.63
180	0		0.20	0.67	0.67
180	90		0.24	0.67	0.67

As expected, these calculations show that:

- the depolarization power Δ is zero when all the elementary matrices remain the same ($\Psi_\delta = 0$, $\Psi_\theta = 0$) whatever the retardance δ_0;
- Δ increases with both Ψ_δ and Ψ_θ. In other words, Δ is higher as the diversity of the elementary matrices is large;

- if the orientation of the eigenaxes remains the same for all the retarders (i.e., $\Psi_\theta = 0$), the increase in Δ as a function of Ψ_δ remains the same whatever the central retardance δ_0;
- for given ranges of variations Ψ_δ and Ψ_θ, the depolarization power Δ increases with δ_0.

We can notice that in this case where only pure retarders are involved, Δ cannot exceed a maximum value $\Delta_{max} = 2/3 \sim 0.67$, as demonstrated in the Appendix A. For reaching higher Δ, the variety of the averaged elementary matrices must be increased by involving additional polarimetric effects, namely circular retardance and linear and circular diatten-uations. Circular retardance φ induced by the sample between incident right and left circular polarizations results in a rotation of the transmitted polarization state by an angle of $-\varphi/2$. Linear diattenuation D_L is given by [19]:

$$D_L = \left| \frac{T_{LH} - T_{LV}}{T_{LH} + T_{LV}} \right| \tag{11}$$

where T_{LH} and T_{LV} are, respectively, the transmission coefficients of linear polarizations oriented, respectively, along the orthogonal diattenuation eigenaxes H and V of the sample. There is no linear diattenuation when $T_{LH} = T_{LV}$ ($D_L = 0$) whereas the sample is a perfect linear diattenuator, i.e., an ideal polarizer, when $T_{LV} = 0$ or $T_{LH} = 0$ ($D_L = 1$). Similarly, circular diattenuation D_c is given by:

$$D_C = \left| \frac{T_{CR} - T_{CL}}{T_{CR} + T_{CL}} \right| \tag{12}$$

where T_{CR} and T_{CL} are the transmission coefficients of incident right and left circular polarizations, respectively.

Circular diattenuation being most of the time negligible in biological samples, we set $D_c = 0$ in the following. Then, to simulate pixels exhibiting both linear and circular retard-ance and linear diattenuation, we numerically built new elementary matrices M, each be-ing the product of three basic matrices, namely, that of a pure linear retarder M_{LR}, that of a pure rotator M_{CR} and that of a pure linear diattenuator M_{LD}, as follows:

$$M = M_{LR}.M_{CR}.M_{LD} \tag{13}$$

This order of the matrices in the product is in accordance with that established in reference papers such as [17] and [42]. For each of these elementary matrices, the linear diattenuation D_L was randomly drawn in a predefined range $\Psi_{DL} = [0; D_{Lmax}]$ and the ori-entation of the eigenaxes of diattenuation was set identical to that of the eigenaxes of re-tardance, as it is generally the case in actual samples. Similarly, for each pixel, the circular retardance φ was drawn in a predefined range $\Psi_\varphi = [0; \varphi_{max}]$. At this point, we can note that the number of parameters involved in the simulations has been significantly in-creased. To help the reader, we list these parameters and we remind their physical signi-fication in Table 2.

In Figure 4, we plot the depolarization power Δ as a function of Ψ_δ and Ψ_θ, for 4 different pairs of Ψ_{DL} and Ψ_φ, the central retardance being $\delta_0 = 45°$ in all cases. Figure 4b,c highlight that the extent of the range of diattenuation has a relatively weak influence on the maximum attainable value of Δ (called Δ_{max} in the following), obtained when $\Psi_\delta = 180°$ and $\Psi_\theta = 180°$. For instance, Δ_{max} only increases from 0.55 to 0.6 when Ψ_{DL} increases from 0.1 to 0.99, with $\Psi_\varphi = 90°$. On the contrary, by comparing Figure 4a,b,d, we can see that Δ_{max} significantly increases as Ψ_φ is increased. For example, Ψ_{DL} being set to 0.1 in all cases, Δ_{max} reaches 0.37, 0.60 and 0.85 when Ψ_φ is set to 10°, 90° and 180°, respectively. These remarks are supported by the data of Table 3, where Δ_{max} is reported as a function of Ψ_{DL} and Ψ_φ. We can notice that, as predictable, Δ_{max} can now exceed the previous maximum value of 0.67. For instance, for $\delta_0 = 45°$ and for the largest variety of polarimetric effects in

the considered pixels (i.e., $\Psi_\delta = 180°$, $\Psi_\theta = 180°$, $\Psi_{DL} = 1$, and $\Psi_\varphi = 180°$), $\Delta_{max} = 0.88$. Δ_{max} can be even more increased, considering higher δ_0. Thus, with $\delta_0 = 90°$ and the same Ψ_δ, Ψ_θ, Ψ_{DL} and Ψ_φ as previously, the calculated Δ_{max} exceeds 0.99, very close to the maximum possible value of 1. However, because circular retardance is likely to be very low in actual biological samples, values of Δ lower than 0.67 should be expected in experimental measurements.

Table 2. Parameters involved in the calculation of the depolarization power when linear retardance, circular retardance, and linear diattenuation occur in each pixel.

δ	Retardance of a given pixel
δ_0	Central retardance of the N considered pixels
Ψ_δ	Extend of the range of the retardances around δ_0 for the N considered pixels
θ	Orientation of the eigen axis of a given pixel
θ_0	Central orientation of the eigen axes of the N considered pixels ($\theta_0 = 0$)
Ψ_θ	Extend of the range of the orientations of the eigen axes around θ_0 for the N considered pixels
D_L	Linear diattenuation of a given pixel
Ψ_{DL}	Extend of the range of the linear diattenuations, from 0 to the maximum value D_{Lmax}, for the N considered pixels (i.e., $\Psi_{DL} = D_{Lmax}$)
φ	Circular retardance of a given pixel
Ψ_φ	Extend of the range of the circular retardances, from 0 to the maximum value φ_{max}, for the N considered pixels (i.e., $\Psi_\varphi = \varphi_{max}$)
Δ	Depolarization power calculated for the N considered pixels, for given δ_0, Ψ_δ, Ψ_θ, Ψ_{DL} and Ψ_φ
Δ_{max}	Maximum attainable depolarization power calculated for the N considered pixels, for given δ_0, Ψ_{DL} and Ψ_φ ($\Psi_\delta = 180°$, $\Psi_\theta = 180°$)

Table 3. Maximum attainable depolarization power Δ_{max} calculated as a function of the variation range of the linear diattenuation Ψ_{DL} and of the variation range of the circular retardance Ψ_φ, in 1000 neighboring pixels ($\delta_0 = 45°$).

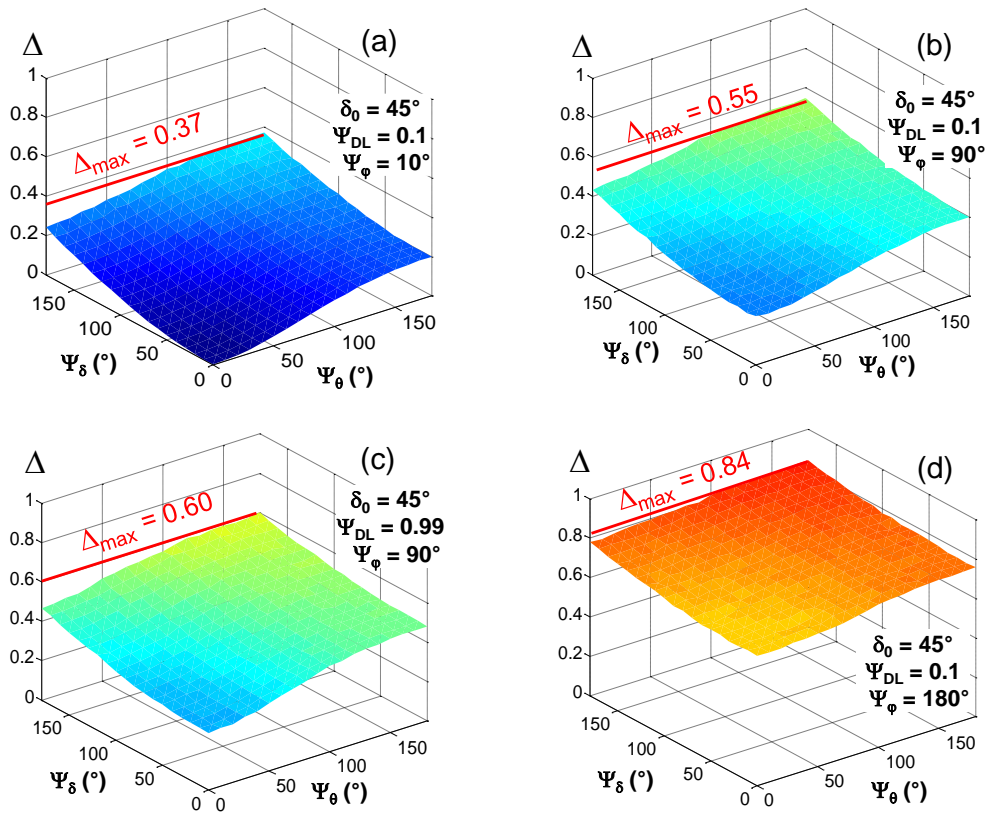| $\Psi_{DL} \rightarrow$	0.	0.1	0.5	0.8	0.99
Ψ_φ (°) $\downarrow$					
0	0.37	0.37	0.38	0.40	0.43
60	0.45	0.46	0.47	0.50	0.51
120	0.65	0.65	0.66	0.69	0.71
180	0.84	0.85	0.85	0.86	0.88

Figure 4. Depolarization power Δ of the average Mueller matrix of 1000 elementary Mueller matrices, each of them being the product of 3 matrices: the matrix of a pure linear retarder, the matrix of a pure circular retarder, and the matrix of a pure linear diattenuator. Δ is calculated as a function of the variation range of the retardance Ψ_δ and of the variation range of the orientation of the eigenaxes Ψ_θ of the linear retarders. The central value of the linear retardance is $\delta_0 = 45°$. The diattenuation of each pixel is randomly drawn within the range $[0; \Psi_{DL}]$ and the circular retardation of each pixel is randomly drawn within the range $[0; \Psi_\varphi]$. (**a**) $\Psi_{DL} = 0.1$ and $\Psi_\varphi = 10°$; (**b**) $\Psi_{DL} = 0.1$ and $\Psi_\varphi = 90°$; (**c**) $\Psi_{DL} = 0.99$ and $\Psi_\varphi = 90°$; (**d**) $\Psi_{DL} = 0.1$ and $\Psi_\varphi = 180°$.

From the above simulations, we can infer that meaningful depolarization power can be measured with the proposed method of averaging Mueller matrices of neighboring pixels, since we have shown that Δ increases as the variety of the involved Mueller matrices is increased.

At this point, it should be noted that, by nature, the calculated Δ are subject to some uncertainty. Indeed, as the polarimetric characteristics of each elementary matrix (δ, θ, D_L and φ) are randomly drawn within a range of some extent (respectively, Ψ_δ, Ψ_θ, Ψ_{DL} and Ψ_φ), the calculated Δ may change when reiterating a given simulation with a new draw. Thus, we achieved some additional simulations in order to evaluate this uncertainty. For this, we repeated M times (M > 100) a given calculation of Δ with M successive draws of the polarimetric characteristics of the elementary matrices and we determined the uncertainty on Δ as being equal to $0.5(\Delta_{max} - \Delta_{min})$, Δ_{max}, and Δ_{min} being, respectively, the highest and the lowest values of Δ obtained over the M repeated simulations. We first fixed the central retardance $\delta_0 = 0°$ and we calculated the maximum uncertainty on Δ versus the number N of averaged matrices, which was obtained in the most unfavorable case, namely, when we considered the largest possible ranges of the retardance ($\Psi_\delta = 180°$), of the orientation of the eigenaxes ($\Psi_\theta = 180°$), of the diattenuation ($\Psi_{DL} = 1$), and of the circular retardation ($\Psi_\varphi = 180°$). Then, we repeated these calculations with δ_0 progressively increased from 0° to 180°, by steps of 10°. Finally, we plot in Figure 5 the highest maximum uncertainty on Δ versus N, noted $\pm \xi(N)$, obtained over the different values of δ_0. This

curve shows that, whatever δ_0, the maximum uncertainty on Δ decreases as N is increased, i.e., Δ converges towards a limit value. With N = 1000, as used in the above simulations, ξ was found to be lower than 0.02. In view of experimental measurements, we considered a floating window of 5 rings of pixels around the central one (N = 121). In this case, ξ was found to remain lower than 0.07. This value is still acceptable, especially if we remember that it is the highest attainable uncertainty obtained in the most unfavorable case with N = 121, which means that actual ξ will be likely to be significantly lower in practical applications. Obviously, ξ could be reduced with higher N, but at the expense of lower resolution of the image. It is the reason why, in further experimental imaging of Δ, we will choose to not exceed this value of N = 121.

We must also notice that, in experimental measurements, the value of Δ obtained with our method may be somewhat different from that obtained with a classical wide-field Mueller polarimeter in free space because the experimental conditions are significantly different, as depicted in Section 1. In the next section, we report and discuss experimental measurements of Δ achieved using our TWDM-based endoscopic Mueller polarimeter and by means of the method of averaging Mueller matrices of neighboring pixels for different depolarizing samples.
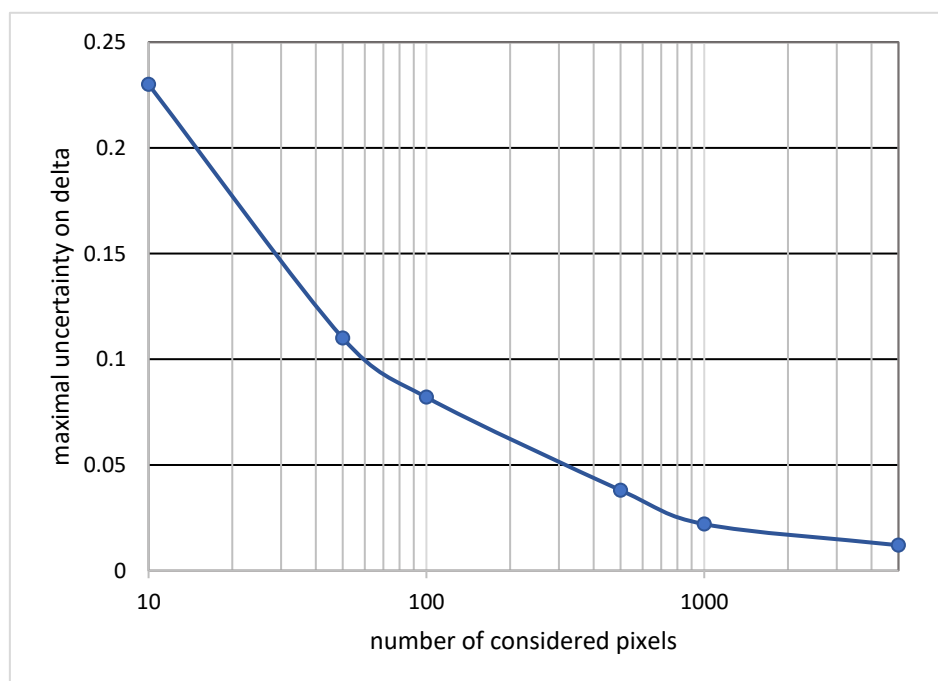

Figure 5. Highest uncertainty on the depolarization power Δ calculated versus the number of averaged elementary matrices, obtained using the largest possible ranges of variations of the polarimetric characteristics of these matrices, and whatever the central value of the retardance.

3. Material and Experimental Results

3.1. Depolarization Measurement on a Manufactured Sample

In order to experimentally evaluate the method of averaging Mueller matrices of neighboring pixels, a reference depolarizing sample should be necessary. However, such a sample exhibiting a predetermined depolarization power does not actually exist. One reason is that the measured depolarization power strongly depends on the experimental conditions of the measurement, as already pointed out in this paper. Another even more important reason is that, in any material, it is extremely difficult to control or manage the magnitude of the diffusion phenomena which are at the origin of spatial depolarization. An exception is Spectralon, produced by Labsphere, North Sutton, NH, USA, which is a highly diffuse material based on polytetrafluoroethylene, and which is widely accepted as a reflectance standard close to a Lambertian surface [43,44]. As such, its polarimetric

characteristics have been widely studied and documented in the literature [45–47]. In particular, it was shown that Spectralon behaves as a pure partial depolarizer, the depolarization power increasing with the reflectance value [48]. For that reason, we chose to use a Spectralon sample with a diffuse reflectance of 99%, i.e., the highest diffuse reflectance of any known materials.

By means of the TWDM-based endoscopic Mueller polarimeter, we first performed a Mueller polarimetric image of a 500 μm × 500 μm area of this Spectralon sample (126 × 126 pixels). Then, each Mueller matrix was first decomposed by the Lu–Chipman method and the linear retardance δ, the orientation of the eigenaxes of retardance θ, the linear diattenuation D_L, and the depolarization power Δ of each pixel were extracted. These polarimetric characteristics are plotted in Figure 6a–d, respectively. We can observe that δ, θ, and D_L drastically change from one pixel to the next. However, as expected, Δ is ~zero in most of the pixels and it remains small (lower than 0.3) in the others. These nonzero values are due to the fact that, Spectralon being highly diffusive material, very low intensity is re-coupled into the fiber and then detected, resulting in degraded signal to noise ratio.
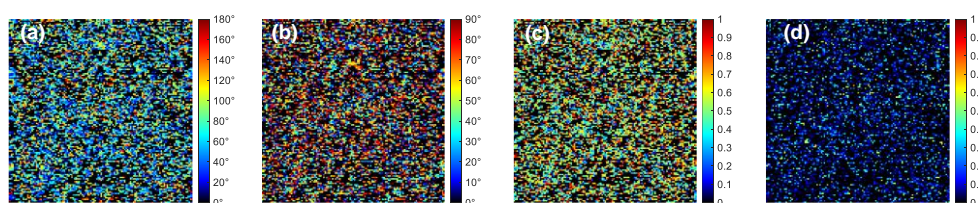

Figure 6. (**a**) linear retardance δ; (**b**) orientation of the eigenaxes of retardance θ; (**c**) linear diattenuation D_L; (**d**) and depolarization power Δ, directly calculated for each pixel of the 126 × 126 Mueller image of a 500 μm × 500 μm area of a Spectralon sample, from the Lu–Chipman decomposition of the corresponding elementary Mueller matrices measured with the TWDM-based endoscopic Mueller polarimeter.

Then, we applied the method of averaging Mueller matrices of neighboring pixels as depicted in Section 2. Figure 7a–c displays the depolarization power calculated for each pixel P of the image, when the considered floating square window around P includes, respectively, *N* = 9 pixels (*n* = 1), 49 pixels (*n* = 3), and 121 pixels (*n* = 5). In these figures, we can notice varied but significant values of Δ which are the signature of the diversity of the polarimetric characteristics displayed in Figure 6. Furthermore, as shown in Figure 7d–f, the standard deviation σ

σ of the distribution of the calculated Δ decreases as the number of pixels included in the floating window increases, i.e., the calculated Δ tends to a value representing the depolarization power of the entire analyzed area.
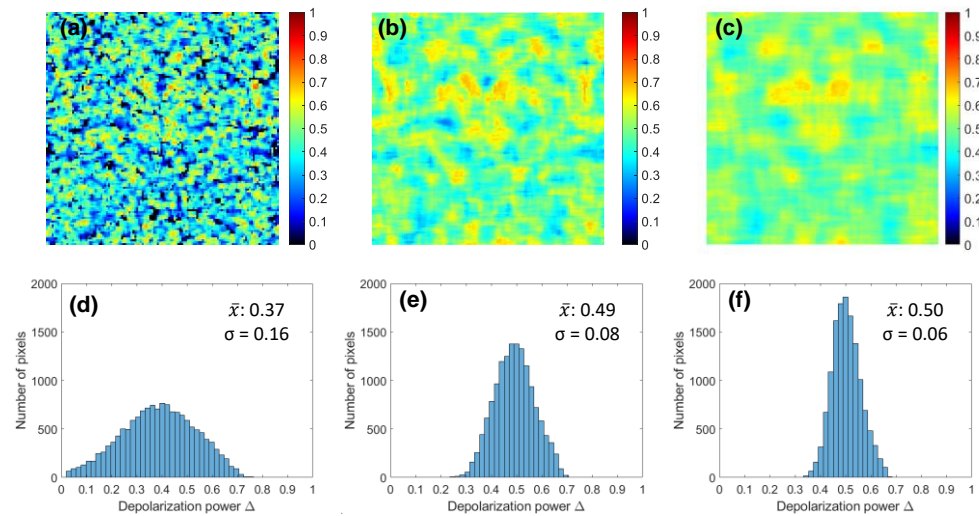
Figure 7. Images of depolarization power of a Spectralon sample (**a**–**c**) and associated histograms (**d**–**f**) calculated by the method of averaging Mueller matrices of neighboring pixels, when considering a floating square window around each pixel containing: (**a**) and (**d**) 9 pixels; (**b**) and (**e**) 49 pixels; (**c**) and (**f**) 121 pixels.

The averaged matrix $\bar{M}$ of all the 126 × 126 = 1576 measured Mueller matrices is the following:

$$\bar{M} = \begin{pmatrix} 1.000 & -0.006 & 0.003 & 0.003 \\ -0.030 & 0.628 & 0.011 & -0.017 \\ -0.012 & 0.005 & 0.610 & 0.003 \\ -0.010 & 0.018 & 0.023 & 0.221 \end{pmatrix} \tag{14}$$

As expected, matrix $\bar{M}$ is very close to the Mueller matrix of a pure partial depolarizer, where coefficients $m_{i,j}$ ($i \neq j$) ~ 0 and coefficients m_{22}, m_{33}, and m_{44} are relatively high but significantly lower than 1. We can notice that the amount of spatial depolarization induced by the Spectralon sample is almost insensitive to the orientation of an incident linear polarization, since $m_{22} \sim m_{33}$. On the other hand, an incident circular polarization experiences higher depolarization from the Spectralon sample than a linear polarization since coefficient m_{44} is significantly lower than coefficients m_{22} and m_{33}. The depolarization power directly calculated from this matrix $\bar{M}$ is equal to 0.51. It is notably lower than that reported in previous papers, regarding similar Spectralon sample with 99% diffuse reflectance [47,48]. This discrepancy can be explained by the fact that the experimental conditions are significantly different in these papers, in particular the size of the region illuminated at the same time which is much larger than in our measurements.

3.2. Depolarization Measurement on a Biological Sample

Afterwards, we achieved the same kind of measurement on a 40 μm thick sample of rat tail tendon (126 × 126 pixels). This biological sample rich in Type-I collagen is likely to exhibit retardance due to the birefringence of the collagen fibers as well as depolarization in the regions where the collagen fibers are disorganized. The linear retardance, the orientation of the eigenaxes, the linear diattenuation, and the depolarization in each pixel of the imaged area were extracted by means of the Lu–Chipman decomposition of the associated Mueller matrix. The corresponding polarimetric images are shown in Figure 8. One more time, we can notice that the measured depolarization power was ~0 for any individual pixel (Figure 8d). Then, we selected two sub-areas in the images of Figure 8, one at the top delimited by white boundaries (so-called sub-area 1) and one at the bottom delimited by red boundaries (so-called sub-area 2). A large diversity of retardance and of eigenaxes

orientation can be seen in sub-area 1, whereas these characteristics are much more similar in sub-area 2. This observation is quantitatively confirmed by means of the histograms reported in Figure 9. In these conditions, one can expect to find higher Δ in sub-area 1 than in sub-area 2, when implementing the method of averaging Mueller matrices of neighboring pixels.
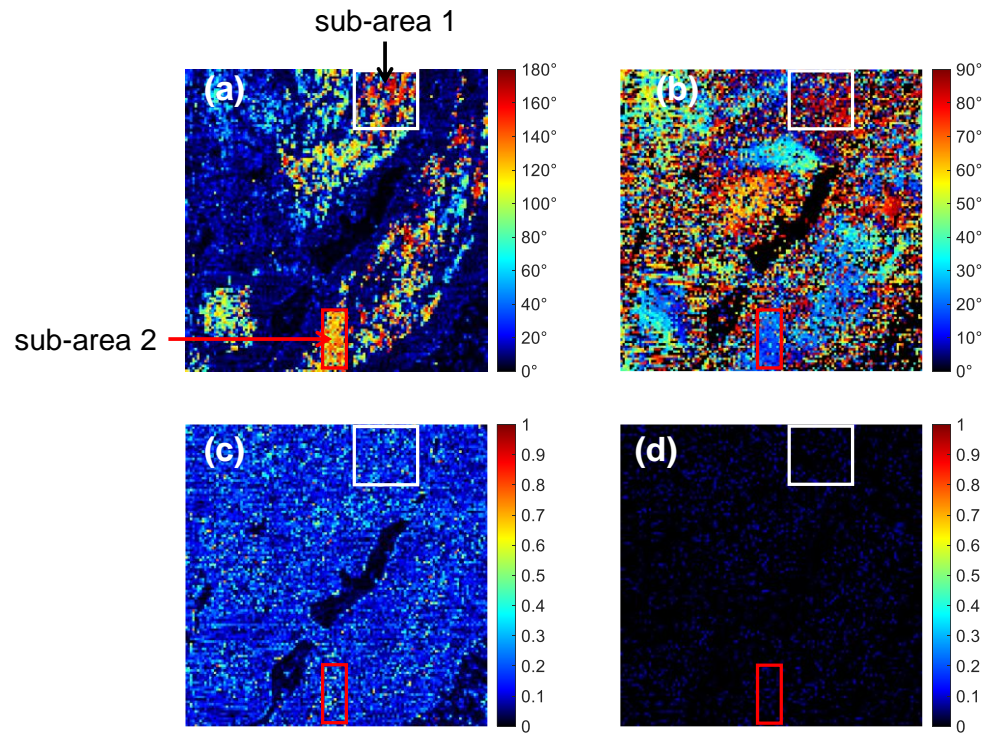

Figure 8. (**a**) linear retardance δ; (**b**) orientation of the eigenaxes of retardance θ; (**c**) linear diattenuation D_L; (**d**) and depolarization power Δ, directly calculated for each pixel of the 126 × 126 Mueller image of a 500 µm × 500 µm area of a rat tail tendon sample, from the Lu–Chipman decomposition of the corresponding elementary Mueller matrices measured with the TWDM-based endoscopic Mueller polarimeter.
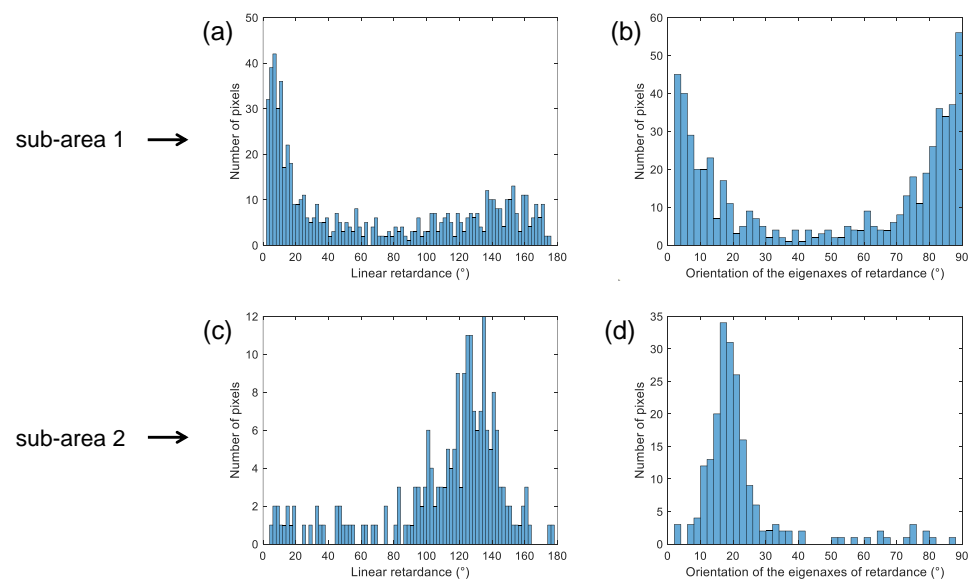

Figure 9. Histograms of the linear retardance (**a**,**c**) and of the orientations of the eigenaxes of retardance (**b**,**d**) in sub-area 1 (**a**,**b**) and in sub-area 2 (**c**,**d**) of the polarimetric images of Figure 8.

As already performed with the Spectralon sample, we applied the method of averaging Mueller matrices of neighboring pixels to calculate the depolarization power associated to each pixel P, when considering a floating square window around P of N = 9 pixels (*n* = 1), 49 pixels (*n* = 3), and 121 pixels (*n* = 5), respectively. The corresponding images are displayed in Figure 10. In sub-area 2, where the polarimetric characteristics of the involved pixels are almost similar, the depolarization power calculated when considering a floating square window of 121 pixels (Figure 10c) is limited to about 0.25. As expected, it is significantly higher in sub-area 1 (up to about 0.6), where the diversity of the polarimetric characteristics of the involved pixels is larger.
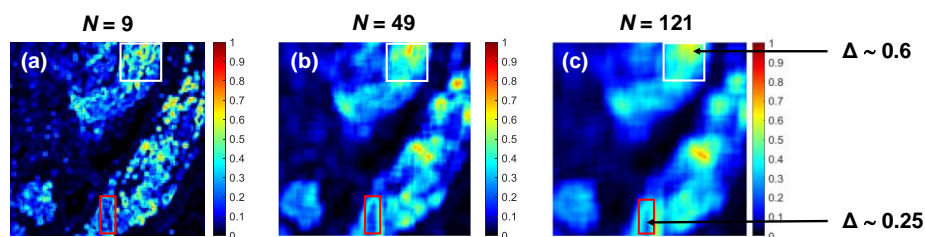

Figure 10. Depolarization power of a rat tail tendon sample calculated by the method of averaging Mueller matrices of neighboring pixels, when considering a floating square window around each pixel of: (**a**) 9 pixels; (**b**) 49 pixels; (**c**) 121 pixels.

The above measurements show that, thanks to the method of averaging Mueller matrices of neighboring pixels, one can calculate depolarization powers representative of the diversity of the polarization states transmitted by the pixels of given sub-areas, and therefore representative of the actual amount of spatial depolarization induced by these sub-areas. Unfortunately, an in-depth quantitative comparison of these values of Δ with others measured by means of a classical wide-field free-space Mueller polarimeter would not really make sense, since the experimental conditions are, by construction, drastically different. Nevertheless, this does not prevent this evaluation of Δ from being of great interest in view of completing the polarimetric characterization of biological tissues achieved by means of our TWDM-based endoscopic Mueller polarimeter, for application to the early diagnosis of certain diseases of inner organs.

4. Conclusions

In this paper, we proposed a method for estimating the depolarization power Δ of a sample, from non-depolarizing Mueller matrices measured through a single-mode fiber endoscope. For each pixel P of the depolarization image, this method founded on the pioneer works by Van de Hulst [39] and later by Gil and Bernabeu [34] consists of:

- calculating a new matrix $\bar{M}$ as the normalized sum of the Mueller matrices of all pixels included in a floating window centered on P;
- performing the polar decomposition of $\bar{M}$ by the Lu–Chipman method;
- calculating Δ from the depolarization matrix resulting from this decomposition.

By means of numerical simulations, we first verified that increasing the diversity of the polarization states from the assembly of considered pixels actually results in increased Δ, as predicted. Then, we used a single-mode fiber-based endoscopic Mueller polarimeter founded on the so-called "Two-Wavelength Differential Method (TWDM)" for measuring the Mueller matrices of all the 126 × 126 pixels of a 500 μm × 500 μm area of a high reflectance standard (Spectralon sample). We showed that the normalized sum of these Mueller matrices was very close to the Mueller matrix of a pure partial depolarizer. Finally, with the same technique, we characterized a biological sample (rat tail tendon). We obtained highly contrasted Δ, from 0.25 to 0.6, depending on the diversity of the polarization states transmitted by the considered sub-areas of this sample. All these results are completely consistent and they are in qualitative good accordance with predictions.

However, because our endoscopic Mueller polarimeter involves an optical fiber for transporting both the probe beam and part of the reflected light, and because this fiber must be single-mode at the working wavelengths, the measurement conditions are very different from those encountered with usual wide-field free-space Mueller polarimeters. On the one hand, only a very small region of the sample is probed at a given time (size of the spot focused on the sample), and on the other hand, the fiber behaves as a very narrow spatial filter on the reflected beam. For these reasons, a significate quantitative comparison with measurements of depolarization reported elsewhere cannot be achieved at this point, and further study regarding such comparison will be necessary. Thus, in the following, this issue will constitute a priority work. Another technical issue to be considered is the frame rate of our endomicroscope which can remain too low for operational use of the technique. Indeed, the current somewhat long 2s duration for one image may result in measurements subject to motion artefacts (heartbeat, patient breath…). Even if this motion could be reduced by pressing the extremity of the microprobe against the targeted tissue, additional research effort should be achieved for increasing the frame rate.

Nevertheless, to our best knowledge, this is the first work allowing complete polarimetric characterization of a sample through a single-mode fiber endoscope, including an estimation of the depolarization. Because this last quantity is of great interest for early diagnosis of certain diseases of biological tissues, this work reinforces the potential of endoscopic Mueller polarimetry in view of performing such diagnoses on inner organs, without biopsy.

Appendix A

Calculation of the maximum depolarization power Δ_{max} attainable with a parallel series of pure retarders with varied retardances δ_i in a range of extend Ψ_δ around a central value δ_0, and with the orientation of their eigenaxes θ_i taken in the range of maximal extend $\Psi_\theta = \pi$.

Let us remember that the Mueller matrix of a pure retarder of retardance δ with its eigenaxes oriented with an angle θ in the reference framework is [14]:

$$M_R = \begin{pmatrix} 1 & 0 & 0 & 0 \\ 0 & A = \cos^2 2\theta + \sin^2 2\theta.\cos\delta & D = \sin 2\theta.\cos 2\theta.(1 - \cos\delta) & E = -\sin 2\theta.\sin\delta \\ 0 & G = \sin 2\theta.\cos 2\theta.(1 - \cos\delta) & B = \sin^2 2\theta + \cos^2 2\theta.\cos\delta & F = \cos 2\theta.\sin\delta \\ 0 & H = \sin 2\theta.\sin\delta & I = -\cos 2\theta.\sin\delta & C = \cos\delta \end{pmatrix} \quad (A1)$$

Let us now consider a uniform random selection of a large number of n retarders R_i ($1 \le i \le n$) with their retardance δ_i taken in a range of extend Ψ_δ around a central value δ_0,

and with the orientation of their eigenaxes θ_i taken in a range of extend Ψ_θ around a central value θ_0, so that: $\delta_0 - \Psi_\delta/2 \le \delta_i \le \delta_0 + \Psi_\delta/2$ and $\theta_0 - \Psi_\theta/2 \le \theta_i \le \theta_0 + \Psi_\theta/2$.

The Mueller matrix of a retarder R_i being noted M_{Ri}, the Mueller matrix of the n retarders in parallel is the mean Mueller matrix of the matrices M_{Ri} ($1 \le i \le n$), noted $\bar{M}$:

$$\bar{M} = \frac{1}{n} \sum_{i=1}^{n} M_{Ri} \tag{A2}$$

$$\bar{M} = \begin{pmatrix} 1 & 0 & 0 & 0 \\ 0 & \bar{A} & \bar{D} & \bar{E} \\ 0 & \bar{G} & \bar{B} & \bar{F} \\ 0 & \bar{H} & \bar{I} & \bar{C} \end{pmatrix} \quad \text{where} \quad \bar{X} = \frac{1}{n} \sum_{i=1}^{n} X_i \qquad X = A, B, \ldots\ldots, I \tag{A3}$$

The maximum depolarization power Δ_{max} of the matrix $\bar{M}$ will be obtained with the largest diversity of the orientations of the eigenaxes, i.e., with $\Psi_\theta = \pi$. Let us calculate the non-diagonal coefficients of $\bar{M}$ (i.e., $\bar{D}, \bar{E}, \bar{F}, \bar{G}, \bar{H}$ and $\bar{I}$) in this case where $\Psi_\theta = \pi$.

$$\bar{D} = \frac{1}{n} \sum_{i=1}^{n} \sin 2\theta_i . \cos 2\theta_i . (1 - \cos \delta_i) \tag{A4}$$

Since the random selection of the parameters δ_i and θ_i is uniform and since we consider a large number of retarders, we can write:

$$\bar{D} \sim \frac{1}{\pi \psi_\delta} \int_{\theta_0 - \frac{\pi}{2}}^{\theta_0 + \frac{\pi}{2}} \int_{\delta_0 - \frac{\psi_\delta}{2}}^{\delta_0 + \frac{\psi_\delta}{2}} \sin 2\theta . \cos 2\theta . (1 - \cos \delta) d\theta d\delta \tag{A5}$$

$$\bar{D} \sim \frac{1}{\pi} \int_{\theta_0 - \frac{\pi}{2}}^{\theta_0 + \frac{\pi}{2}} \sin 2\theta . \cos 2\theta d\theta \times \frac{1}{\psi_\delta} \int_{\delta_0 - \frac{\psi_\delta}{2}}^{\delta_0 + \frac{\psi_\delta}{2}} (1 - \cos \delta) d\delta \tag{A6}$$

Using the relationship $\sin a . \cos a = \dfrac{\sin 2a}{2}$, Equation (A6) becomes:

$$\bar{D} \sim \frac{1}{2\pi} \int_{\theta_0 - \frac{\pi}{2}}^{\theta_0 + \frac{\pi}{2}} \sin 4\theta d\theta \times \frac{1}{\psi_\delta} \int_{\delta_0 - \frac{\psi_\delta}{2}}^{\delta_0 + \frac{\psi_\delta}{2}} (1 - \cos \delta) d\delta \tag{A7}$$

The left integral of Equation (A7) being zero, we finally obtain $\bar{D} = 0$ and as $\bar{G} = \bar{D}$, we deduce that $\bar{G} = 0$.

Similarly, we calculate $\bar{E}$ with:

$$\bar{E} \sim \frac{1}{\pi \psi_\delta} \int_{\theta_0 - \frac{\pi}{2}}^{\theta_0 + \frac{\pi}{2}} \int_{\delta_0 - \frac{\psi_\delta}{2}}^{\delta_0 + \frac{\psi_\delta}{2}} -\sin 2\theta . \cos \delta d\theta d\delta = \frac{-1}{\pi} \int_{\theta_0 - \frac{\pi}{2}}^{\theta_0 + \frac{\pi}{2}} \sin 2\theta d\theta \times \frac{1}{\psi_\delta} \int_{\delta_0 - \frac{\psi_\delta}{2}}^{\delta_0 + \frac{\psi_\delta}{2}} \cos \delta d\delta \tag{A8}$$

The left integral of Equation (A8) is zero, so that $\bar{E} = 0$, and as $\bar{H} = -\bar{E}$, we deduce that $\bar{H} = 0$.

Finally, we calculate $\bar{F}$ with:

$$\bar{F} \sim \frac{1}{\pi\psi_\delta} \int\limits_{\theta_0-\frac{\pi}{2}}^{\theta_0+\frac{\pi}{2}} \int\limits_{\delta_0-\frac{\psi_\delta}{2}}^{\delta_0+\frac{\psi_\delta}{2}} \cos 2\theta.\cos\delta\, d\theta\, d\delta = \frac{1}{\pi} \int\limits_{\theta_0-\frac{\pi}{2}}^{\theta_0+\frac{\pi}{2}} \cos 2\theta\, d\theta \times \frac{1}{\psi_\delta} \int\limits_{\delta_0-\frac{\psi_\delta}{2}}^{\delta_0+\frac{\psi_\delta}{2}} \cos\delta\, d\delta \tag{A9}$$

The left integral of Equation (A9) is zero, so that $\bar{F} = 0$, and as $\bar{I} = -\bar{F}$, we deduce that $\bar{I} = 0$.

Since $\bar{D} = \bar{E} = \bar{F} = \bar{G} = \bar{H} = \bar{I} = 0$, Equation (A3) becomes:

$$\bar{M} = \begin{pmatrix} 1 & 0 & 0 & 0 \\ 0 & \bar{A} & 0 & 0 \\ 0 & 0 & \bar{B} & 0 \\ 0 & 0 & 0 & \bar{C} \end{pmatrix} \tag{A10}$$

$\bar{M}$ is the Mueller matrix of a pure partial depolarizer which depolarization power is [19]:

$$\Delta_{max} = 1 - \frac{|\bar{A}| + |\bar{B}| + |\bar{C}|}{3} \tag{A11}$$

Let us now calculate $|\bar{A}|$, $|\bar{B}|$ and $|\bar{C}|$.

$$\bar{A} = \frac{1}{n} \sum_{i=1}^{n} (\cos^2 2\theta_i + \sin^2 2\theta_i.\cos\delta_i) \tag{A12}$$

As we proceeded for the previous quantities, we can write:

$$\bar{A} \sim \frac{1}{\pi} \int\limits_{\theta_0-\frac{\pi}{2}}^{\theta_0+\frac{\pi}{2}} \cos^2 2\theta\, d\theta + \frac{1}{\pi} \int\limits_{\theta_0-\frac{\pi}{2}}^{\theta_0+\frac{\pi}{2}} \sin^2 2\theta\, d\theta.\frac{1}{\psi_\delta} \int\limits_{\delta_0-\frac{\psi_\delta}{2}}^{\delta_0+\frac{\psi_\delta}{2}} \cos\delta\, d\delta$$

$$= \frac{1}{2\pi} \int\limits_{\theta_0-\frac{\pi}{2}}^{\theta_0+\frac{\pi}{2}} (1+\cos 4\theta)\, d\theta + \frac{1}{2\pi} \int\limits_{\theta_0-\frac{\pi}{2}}^{\theta_0+\frac{\pi}{2}} (1-\cos 4\theta)\, d\theta.\frac{1}{\psi_\delta} \int\limits_{\delta_0-\frac{\psi_\delta}{2}}^{\delta_0+\frac{\psi_\delta}{2}} \cos\delta\, d\delta \tag{A13}$$

$$= \frac{1}{2} + \frac{1}{2\psi_\delta}\left(\sin\left(\delta_0+\frac{\psi_\delta}{2}\right) - \sin\left(\delta_0-\frac{\psi_\delta}{2}\right)\right) = \frac{1}{2} + \frac{1}{\psi_\delta}\sin\frac{\psi_\delta}{2}.\cos\delta_0$$

$$= \frac{1}{2}\left(1 + \frac{\sin\dfrac{\psi_\delta}{2}}{\dfrac{\psi_\delta}{2}}.\cos\delta_0\right)$$

Similarly, we can calculate:

$$\bar{B} = \frac{1}{2} + \frac{1}{\psi_\delta}\sin\frac{\psi_\delta}{2}.\cos\delta_0 \qquad = \frac{1}{2}\left(1 + \frac{\sin\dfrac{\psi_\delta}{2}}{\dfrac{\psi_\delta}{2}}.\cos\delta_0\right) \tag{A14}$$

and

$$\bar{C} = \frac{\sin\dfrac{\psi_\delta}{2}}{\dfrac{\psi_\delta}{2}}.\cos\delta_0 \tag{A15}$$

With $0 \le \psi_\delta \le \pi$ and $0 \le \delta_0 \le \pi$ we can note that $\bar{A} = \bar{B} \ge 0$ and then $\left|\bar{A}\right| = \bar{A}$ and $\left|\bar{B}\right| = \bar{B}$.

In the case where $0 \le \delta_0 \le \dfrac{\pi}{2}$, $\bar{C} \ge 0$ and then $\left|\bar{C}\right| = \bar{C}$. In that case, from Equations (A13)–(A15), we can deduce that:

$$\left|\bar{A}\right| + \left|\bar{B}\right| + \left|\bar{C}\right| = 1 + \frac{\sin \dfrac{\psi_\delta}{2}}{\dfrac{\psi_\delta}{2}} \cos \delta_0$$

And finally, from Equation (A11):

$$\Delta_{max} = \frac{2}{3}\left(1 - \frac{\sin \dfrac{\psi_\delta}{2}}{\dfrac{\psi_\delta}{2}} \cos \delta_0\right)$$

The maximum value of Δ_{max} is reached when $\delta_0 = \pm\dfrac{\pi}{2}$, whatever Ψ_δ. This maximum value is $\dfrac{2}{3}$.

In the case where $\dfrac{\pi}{2} \le \delta_0 \le \pi$, $\bar{C} \le 0$ and then $\left|\bar{C}\right| = -\bar{C}$. In that case, from Equations (A13)–(A15), we can deduce that:

$$\left|\bar{A}\right| + \left|\bar{B}\right| + \left|\bar{C}\right| = 1$$

and from Equation (A11), we deduce that $\Delta_{max} = \dfrac{2}{3}$, whatever $\delta_0 \ge \dfrac{\pi}{2}$ and whatever Ψ_δ.

References

1. Jacques, S.; Ramella-Roman, J.; Lee, K. Imaging skin pathology with polarized light. *J. Biomed. Opt.* **2002**, *7*, 329–340.
2. Ghosh, N.; Vitkin, I.A. Tissue polarimetry: Concepts, challenges, applications, and outlook. *J. Biomed. Opt.* **2011**, *16*, 110801.
3. Vitkin, A.; Ghosh, N.; De Martino, A. Tissue Polarimetry. In *Photonics: Biomedical Photonics, Spectroscopy and Microscopy*; John Wiley and Sons: Hoboken, NJ, USA, 2015.
4. Tuchin, V.V. Polarized light interaction with tissues. *J. Biomed Opt.* **2016**, *21*, 071114.
5. Yasui, T.; Tohno, Y.; Araki, T. Determination of collagen fiber orientation in human tissue by use of polarization measurement of molecular second-harmonic-generation light. *Appl. Opt.* **2004**, *43*, 2861–2867.
6. Bancelin, S.; Nazac, A.; Ibrahim, B.H.; Dokládal, P.; Decencière, E.; Teig, B.; Haddad, H.; Fernandez, H.; Schanne-Klein, M.-C.; De Martino, A. Determination of collagen fiber orientation in histological slides using Mueller microscopy and validation by second harmonic generation imaging. *Opt. Express* **2014**, *22*, 22561–22574.
7. Chipman, R.A. Polarimetry. In *Handbook of Optics Volume II*; McGraw-Hill: New York, NY, USA, 1995.
8. Wood, M.F.G.; Ghosh, N.; Wallenburg, M.A.; Li, S.-H.; Weizel, R.D.; Wilson, B.C.; Li, R.-K.; Vitkin, I.A. Polarization birefringence measurements for characterizing the myocardium, including healthy, infarcted, and stem-cell-regenerated tissues. *J. Biomed. Opt.* **2010**, *15*, 047009.
9. Pierangelo, A.; Benali, A.; Antonelli, ; Novikova, T.; Validire, P.; Gayet, B.; De Martino, A. Ex-vivo characterization of human colon cancer by Mueller polarimetric imaging. *Opt. Express* **2011**, *19*, 1582–1593.
10. Dubreuil, M.; Babilotte, P.; Martin, L.; Sevrain, D.; Rivet, S.; Le Grand, Y.; Le Brun, G.; Turlin, B.; Le Jeune, B. Mueller matrix polarimetry for improved liver fibrosis diagnosis. *Opt. Lett.* **2012**, *37*, 1061–1063.
11. Jagtap, J.; Chandel, S.; Das, N.; Soni, J.; Chatterjee, S.; Pradhan, A.; Ghosh, N. Quantitative Mueller matrix fluorescence spectroscopy for precancer detection. *Opt. Lett.* **2014**, *39*, 243–246.
12. Qi, J.; Alson, D.S. Mueller polarimetric imaging for surgical and diagnostic applications: A review. *J. Biophotonics* **2017**, *10*, 950–982.
13. Kupinski, M.; Boffety, M.; Goudail, F.; Ossikovski, R.; Pierangelo, A.; Rehbinder, J.; Vizet, J.; Novikova, T. Polarimetric measurement utility for pre-cancer detection from uterine cervix specimens. *Biomed. Opt. Express* **2018**, *9*, 5691–5702.
14. Goldstein, D.H. Mueller Matrix Polarimetry. In *Polarized Light*, 3rd ed.; CRC Press: Boca Raton, FL, USA, 2011.

15. Morio, J.; Goudail, F. Influence of the order of diattenuator, retarder, and polarizer in polar decomposition of Mueller matrices. *Opt. Lett.* **2004**, *29*, 2234–2236.

16. Ossikovski, R. Analysis of depolarizing Mueller matrices through a symmetric decomposition. *J. Opt. Soc. Am. A* **2009**, *26*, 1109–1118.

17. Vizet, J.; Ossikovski, R. Symmetric decomposition of experimental depolarizing Mueller matrices in the degenerate case. *Appl. Opt.* **2018**, *57*, 1159–1167.

18. Gil, J.J.; San José, I. Arbitrary decomposition of a Mueller matrix. *Opt. Lett.* **2019**, *44*, 5715–5718.

19. Lu, S.Y.; Chipman, R.A. Interpretation of Mueller matrices based on polar decomposition. *JOSA A* **1996**, *13*, 1106–1113.

20. Desroches, J.; Pagnoux, D.; Louradour, F.; Barthélémy, A. Fiber-optic device for endoscopic polarization imaging. *Opt. Lett.* **2009**, *34*, 3409–3411.

21. Fade, J.; Alouini, M. Depolarization remote sensing by orthogonality breaking. *Phys. Rev. Lett.* **2012**, *109*, 043901.

22. Vizet, J.; Brevier, J.; Desroches, J.; Barthélémy, A.; Louradour, F.; Pagnoux, D. One shot endoscopic polarization measurement device based on a spectrally encoded polarization states generator. *Opt. Express* **2015**, *23*, 16439–16448.

23. Forward, S.; Gribble, A.; Alali, S.; Lindenmaier, A.A.; Vitkin, I.A. Flexible polarimetric probe for 3 × 3 Mueller matrix measurements of biological tissue. *Sci. Rep.* **2017**, *7*, 11958.

24. Fu, Y.; Huang, Z.; He, H.; Ma, H.; Wu, J. Flexible 3 × 3 Mueller matrix endoscope prototype for cancer detection. *IEEE Trans. Instrum. Meas.* **2018**, *67*, 1700–1712.

25. Vizet, J.; Manhas, S.; Tran, J.; Validire, P.; Benali, A.; Garcia-Caurel, E.; Pierangelo, A.; De Martino, A.; Pagnoux, D. Optical fiber-based full Mueller polarimeter for endoscopic imaging using a two-wavelength simultaneous measurement method. *J. Biomed. Opt.* **2016**, *21*, 071106.

26. Buckley, C.; Fabert, M.; Kinet, D.; Kucikas, V.; Pagnoux, D. Design of an endomicroscope including a resonant fiber-based microprobe dedicated to endoscopic polarimetric imaging for medical diagnosis. *Biomed. Opt. Express* **2020**, *11*, 7032–7052.

27. Van Eeckhout, A.; Garcia-Caurel, E.; Ossikovski, R.; Lizana, A.; Rodriguez, C.; González-Arnay, E.; Campos, J. Depolarization metric spaces for biological tissues classification. *J. Biophotonics* **2020**, *13*, e202000083.

28. Rehbinder, J.; Vizet, J.; Park, J.; Ossikovsk, R.; Vanel, J.C.; Nazac, A.; Pierangelo, A. Depolarization imaging for fast and non-invasive monitoring of cervical microstructure remodeling in vivo during pregnancy. *Sci. Rep.* **2022**, *12*, 1232.

29. Du, E.; He, H.; Zeng, N.; Sun, M.; Guo, Y.; Wu, S.; Liu, S.; Ma, H. Mueller matrix polarimetry for differentiating characteristic features of cancerous tissues. *J. Biomed. Opt.* **2014**, *19*, 076013.

30. Zhou, X.; Maloufi, S.; Louie, D.C.; Zhang, N.; Liu, Q.; Lee, T.K.; Tang, S. Investigating the depolarization property of skin tissue by degree of polarization uniformity contrast using polarization-sensitive optical coherence tomography. *Biomed. Opt. Express* **2021**, *12*, 5073–5088.

31. Ushenko, V.A.; Hogan, B.T.; Dubolazov, A.; Piavchenko, G.; Kuznetsov, S.; Ushenko, A.G.; Ushenko, Y.O.; Gorsky, M.; Bykov, A.; Meglinski, I. 3D Mueller matrix mapping of layered distributions of depolarisation degree for analysis of prostate adenoma and carcinoma diffuse tissues. *Sci. Rep.* **2021**, *11*, 5162.

32. Novikova, T.; Pierangelo, A.; de Martino, A.; Benali, A.; Validire, P. Polarimetric imaging for cancer diagnosis and staging. *Opt. Photonics News* **2012**, *13*, 26–33.

33. Ivanov, D.; Dremin, V.; Borisova, E.; Bykov, A.; Novikova, T.; Meglinski, I.; Ossikovski, R. Polarization and depolarization metrics as optical markers in support to histopathology of ex vivo colon tissue. *Biomed Opt. Express* **2021**, *12*, 4560–4572.

34. Gil, J.J.; Bernabeu, E. A Depolarization Criterion in Mueller Matrices. *Opt. Acta Int. J. Opt.* **1985**, *32*, 259–261.

35. Goldstein, D.H. Stokes Polarization Parameters. In *Polarized Light*, 3rd ed.; CRC Press: Boca Raton, FL, USA, 2011.

36. Chipman, R.A. Depolarization. In *Polarization: Measurement, Analysis, and Remote Sensing II*; Proceedings of SPIE 3754; SPIE: Bellingham, WA, USA, 1999; pp. 14–20.

37. Cloud, S.R. Group theory and polarization algebra. *Optik* **1986**, *75*, 26–36.

38. Ortega-Quijano, N.; Fanjul-Vélez, F.; Arce-Diego, J.L. Physically meaningful depolarization metric based on the differential Mueller matrix. *Opt. Lett.* **2015**, *40*, 3280–3283.

39. Van de Hulst, H.C. *Light Scattering by Small Particles*; John Wiley and Sons: New York, NY, USA, 1957.

40. Götzinger, E.; Pircher, M.; Geitzenauer, W.; Ahlers, C.; Baumann, B.; Michels, S.; Schmidt-Erfurth, U.; Hitzenberger, C.K. Retinal pigment epithelium segmentation by polarization sensitive optical coherence tomography. *Opt. Express* **2008**, *16*, 16410–16422.

41. Götzinger, E.; Pircher, M.; Baumann, B.; Ahlers, C.; Geitzenauer, W.; Schmidt-Erfurth, U.; Hitzenberger, C.K. Three-dimensional polarization sensitive OCT imaging and interactive display of the human retina. *Opt. Express* **2009**, *17*, 4151–4165.

42. Ghosh, N.; Wood, M.F.; Vitkin, I.A. Mueller matrix decomposition for extraction of individual polarization parameters from complex turbid media exhibiting multiple scattering, optical activity, and linear birefringence. *J. Biomed. Opt.* **2008**, *13*, 044036.

43. Voss, K.J.; Zhang, H. Bidirectional reflectance of dry and submerged Labsphere Spectralon plaque. *Appl. Opt.* **2006**, *45*, 7924–7927.

44. Bhandari, A.A.; Hamre, B.; Frette, Ø.; Zhao, L.; Stamnes, J.J.; Kildemo, M. Bidirectional reflectance distribution function of Spectralon white reflectance standard illuminated by incoherent unpolarized and plane-polarized light. *Appl. Opt.* **2011**, *50*, 2431–2442.

45. Svensen, Ø.; Kildemo, M.; Maria, J.; Stamnes, J.J.; Frette, Ø. Mueller matrix measurements and modeling pertaining to Spectralon white reflectance standards. *Opt. Express* **2012**, *20*, 15045–15053.

46. Kildemo, M.; Maria, J.; Ellingsen, P.G.; Aas, L.M.S. Parametric model of the Mueller matrix of a Spectralon white reflectance standard deduced by polar decomposition techniques. *Opt. Express* **2013**, *21*, 18509–18524.

47. Dupont, J.; Orlik, X.; Ceolato, R.; Dartigalongue, T. Spectralon spatial depolarization: Towards an intrinsic characterization using a novel phase shift distribution analysis. *Opt. Express* **2017**, *25*, 9544–9555.

48. Sanz, J.M.; Extremiana, C.; Saiz, J.M. Comprehensive polarimetric analysis of Spectralon white reflectance standard in a wide visible range. *Appl. Opt.* **2013**, *52*, 6051–6062.